AMS Home   Journals Home   Journal Archive   Subscribe   For Authors   Help   Advanced Search   [Search] Go

Full Text View

Stratified Flow along a Corrugated Slope: Separation Drag and Wave Drag

Parker MacCready and Geno Pawlak

School of Ocenography, University of Washington, Seattle, Washington

ABSTRACT

Lee wave generation and horizontal flow separation in stratified flow along a slope, with corrugations or a ridge running directly downslope, are explored using analytical and numerical methods. Both of these processes are important to the drag on alongslope currents. The analytical solution for steady wave generation by stratified flow along a corrugated slope is extended to the evanescent flow regimes. There are two evanescent regimes, having intrinsic frequencies either above the buoyancy frequency N (fast flow), or below $N \sin(a)$ (slow flow), for nonrotating fluid and slope angle, $a.$ Streamlines of the low speed evanescent solution tend to follow isobaths, while those of wave solutions tend to flow up over ridges and down in canyons. An analytical expression is developed for the wave drag felt by an isolated ridge on a slope. For a Gaussian ridge of alongslope length $L,$ the drag becomes small when $U/LN > 1$ (the fast flow regime), or when $U/(LN \sin a) < 1/2$ (the slow flow regime).

Numerical experiments are performed for stratified flow along a slope with an isolated ridge. The ridge height is varied and the pressure drag on the ridge evaluated for flow in the wave-generating and slow evanescent regimes. The slow-flow case gives rise to a large region of horizontal (isopycnal) flow separation with proportionally stronger relative vorticity in the wake than the wave-generating case. Pressure drag coefficients based on projected frontal area are similar for both cases, increase linearly with the corrugation amplitude, and level off around a value of 1–1.2.

1. Introduction

Flow at the margins of ocean basins is highly complex. Steep slopes (relative to f/N) rise through the full depth of the ocean and are creased with deep canyons and ridges at many scales. Currents at all frequencies are generally enhanced

there, forcing strong turbulent mixing at and near the boundary. An issue of particular importance is the rate at which oceanic fluid from the "interior" is exchanged with fluid at the sloping boundary. This exchange may improve the efficiency of boundary mixing (Armi 1979), allowing it to contribute significantly to the global overturning circulation (Garrett et al. 1993). Horizontal exchange is also a key process shaping the biological habitat of the coastal region. Horizontal eddies disperse biological communities, chemicals, and pollution within shallow inlets and estuaries, along the continental shelf, and across the shelf break (e.g., Hickey 1998).

Much detailed work has been done on isolated seamounts (Roden and Taft 1985; Boyer and Zhang 1990; Smith 1992; Kunze and Sanford 1993; Codiga 1993, 1997). The canyon is another class of rough topography that has been studied (Chapman and Gawarkiewicz 1995; Alvarez et al. 1996; Codiga et al. 1999; Allen 2000). In addition, the basic boundary layer dynamics of rotating, stratified flow along a planar slope are fairly well understood (MacCready and Rhines 1991, 1993; Trowbridge and Lentz 1991; Lentz and Trowbridge 1991). In this paper we focus on the case of a slope with simple forms of roughness: either corrugation or a single ridge extending down a planar slope. Fundamental work on internal wave generation and form drag has been done recently for the corrugated case by Thorpe (1992, 1996). Here we extend Thorpe's analysis to slower, more horizontal flows, and to isolated ridges. Horizontal flow separation is important in this regime, and we use the work of Signell and Geyer (1991, hereafter SG) as a starting point. They considered the generation of tidal headland eddies in shallow ($\sim$ 20 m) water. We consider the case of flow past a ridge in deeper, stratified waters. In this case friction is much less important for eddy evolution, and internal-wave generation may be important.

While the ocean margins have huge variability in all their properties, some scales may still be considered typical. The slope of the continental slope around the United States, at scales greater than 40 km, ranges between 1:100 and 1:13, but the median slopes at 300-m scales are considerably steeper, from 1:28 to 1:10 (Pratson and Haxby 1996). Another measure of "roughness" important to flows constrained to be mostly horizontal by stratification is the shape of isobaths. It is apparent from any bathymetry chart that isobaths are highly curved on many scales, and there is no consensus in physical oceanography about which scale of topographic feature flow will tend to follow or separate. Even the vocabulary for describing isobath shapes is not well developed. Fluvial geomorphologists define the property of "sinuosity" as the length of a river channel divided by the length of a straight line connecting the ends of the channel. Signell and Geyer used the term "aspect ratio" to mean the ratio of the offshore width of a headland to its alongshore length. We follow their definition but use the more general term "isobath aspect ratio" to describe horizontal shapes of isobaths (whether from an isolated ridge, corrugation, or other arbitrary topographic deviation from a planar slope). We use the term "vertical aspect ratio" to describe the ratio of the height of a topographic feature on the slope to its alongslope length.

The energy of near-margin currents is often dominated by diurnal and semidiurnal tidal motion. The barotropic tide driving these motions is often very weak, but the internal tide may be stronger (5–20 cm s^{-1}) and more aligned with bathymetric contours (Torgrimson and Hickey 1979; White 1994; Petruncio et al. 1998). In regions of topographic channeling of the flow, such as through straits and shallow coastal seas, the barotropic tidal currents may be much larger, and speeds of 1 m s^{-1} are not uncommon (Robinson 1983; Cannon and Bretschineder 1986; SG; Ott and Garrett 1998).

One goal of this paper is to identify topographic features that are most likely to cause flow separation and generate significant horizontal stirring. We focus on situations that are deep relative to the shallow coastal sea studied by SG, but are still close enough to the surface to have large slopes, stratification, and currents. Typical ocean stratification has buoyancy frequencies of 10^{-2} s^{-1} in the upper water column, and 10^{-3} s^{-1} in the abyss.

In section 2 the internal wave and evanescent analytical solutions for steady stratified flow along a corrugated slope are derived. These provide guidance as to which flows are most likely to go around versus over a given corrugation. In section 3 an expression for the pressure drag due to internal wave generation is derived, and the analytical theory is extended to the case of an isolated ridge. Section 4 presents results from 3D numerical simulations of stratified flow along a slope with a single Gaussian ridge, including calculation of the pressure drag and energetics. Results are summarized in section 5.

2. Internal wave and evanescent analytical solutions

Internal wave generation and form stress associated with stratified flow over a flat plane with corrugations, ridges, or isolated bumps has been an active research topic, particularly for atmospheric flows. Results are summarized in Gill (1982) and Baines (1995). Thorpe (1992, 1996) extended the wave generation problem to flow along a corrugated slope. His solution includes the effects of earth rotation and allows for corrugations that are at some angle to the direction of steepest slope. For nonrotating flow with corrugations running purely downslope (Fig. 1 ⊙▣), Thorpe finds two fundamental differences between the sloping and nonsloping problems. First, the group velocity in the sloping case always has a component upslope; thus the effects of form drag will most likely be felt in the shallow nearshore region (e.g., on the continental shelf) where wave energy is dissipated. Second, and of importance to our investigation, there is a "low speed cutoff," a speed below which internal waves are no longer generated.

Here we present an alternate derivation of Thorpe's wave solution and extend it to the evanescent flows above and below

the low speed cutoff. Finally we consider the wave drag due to an isolated ridge running down the slope.

The linearized, Boussinesq equations of momentum, volume, and density conservation for nonrotating, inviscid, incompressible, nonhydrostatic flow may be written as

$$\mathbf{u}_t = -\frac{1}{\rho_o}\nabla p - \hat{\mathbf{k}}\frac{g\rho'}{\rho_o}, \qquad (2.1)$$

$$\nabla \cdot \mathbf{u} = 0, \qquad (2.2)$$

$$\rho'_t + w\overline{\rho}_z = 0, \qquad (2.3)$$

where $\mathbf{u} = (u, \mathbf{v}, w)$ is the velocity vector; subscripts x, y, z, and t denote partial differentiation; $\nabla = (\partial/\partial x, \partial/\partial y, \partial/\partial z)$ is the gradient operator; ρ_o is a constant reference density; $\hat{\mathbf{k}}$ is the vertical unit vector; and g is the acceleration of gravity. The density and pressure have been divided into mean, mean gradient, and perturbation portions:

$$\rho = \rho_o + \overline{\rho}(z) + \rho'(\mathbf{x}, t), \qquad (2.4)$$

$$p = \overline{p}(z) + p'(\mathbf{x}, t). \qquad (2.5)$$

a. Wave solutions

From Eqs. (2.1)–(2.3) we find the standard internal wave equation

$$(\nabla^2 w)_{tt} + N^2\nabla^2_H w = 0. \qquad (2.6)$$

For a wave of the form

$$w = \text{Re}A \, \text{exp}i(kx + ly + mz - \sigma t), \qquad (2.7)$$

the dispersion relation is

$$\sigma^2 = \frac{N^2(k^2 + l^2)}{k^2 + l^2 + m^2} = N^2 \cos^2\theta, \qquad (2.8)$$

where $\mathbf{k} = (k, l, m)$ is the wavenumber vector and θ is the angle of elevation of that vector from the horizontal. Flow is along "phase planes" normal to $\mathbf{k}$, and the group velocity is along the direction of steepest descent of the phase plane (Lighthill 1978).

Now consider internal waves generated by a corrugated boundary with mean slope a, moving in the positive alongslope direction with speed U (Fig. 1 ◯). The corrugations have alongslope wavenumber k and vertical amplitude δ_V (V referring to vertical). Waves generated by a moving boundary under quiescent fluid are, of course, identical to those generated by flow along a stationary boundary. For consistency with the derivation in Gill (1982, section 6.8) we choose to use a moving boundary. The approximate kinematic boundary condition on the vertical velocity is

$$w = \eta_t + u\eta_x + v\eta_y \quad \text{on } z = \eta \cong \alpha y, \qquad (2.9)$$

where η is the topographic elevation, given by

$$\eta = \delta_V \cos[k(x - Ut)] + \alpha y \qquad (2.10)$$

and $\alpha = \tan(a)$. The b.c. may be written as

$$w = Uk\delta_V \sin[k(x - Ut) + \alpha v \quad \text{on } z = \alpha y \qquad (2.11)$$

if we assume $u \ll U$. We will check the consistency of this and other linearizing approximations in section 2c, after we have the full solution. The solution must have x-wavenumber k, frequency $\sigma = kU$, and $l = -\alpha m$ in order to match the

boundary condition, so we limit potential solutions to w for the wave problem to

$$w = w_o \sin[k(x - Ut) + m(z - \alpha y)]. \quad (2.12)$$

Using (2.12) in the boundary condition (2.11) we find

$$w_o \sin[k(x - Ut)] = Uk\delta_V \sin[k(x - Ut)] + \alpha \upsilon|_{z=\alpha y}. \quad (2.13)$$

We need to solve for υ before w is fully determined. Before we do this, however, it is useful to solve for the vertical wavenumber m. Using information about σ and l we may rewrite the dispersion relation (2.8) as

$$F^2 = \frac{k^2 + \alpha^2 m^2}{k^2 + \alpha^2 m^2 + m^2}, \quad (2.14)$$

where $F \equiv Uk/N$ is the Froude number, or the ratio of frequencies, σ/N. Note that without loss of generality we may assume $\sigma > 0$; so for positive U, k will also be positive. We may rewrite (2.14) as

$$m^2 = \frac{k^2(1 - F^2)}{F^2 - \alpha^2(1 - F^2)}. \quad (2.15)$$

For real m we require $(1 - F^2) > 0$ and hence $F < 1$. This gives the usual high-speed cutoff $U < N/k$ for which phase surfaces become vertical. For the sloping case there is also a low-speed cutoff due to the requirement $[F^2 - \alpha^2(1 - F^2)] > 0$ in (2.15). This requirement may be rewritten as $F > \sin(a)$. The cutoff frequency is $\sigma = N \sin(a)$, the natural oscillation frequency of water parcels along the slope angle. Thus, for wave solutions (with real m and hence real l) we require

$$\sin(a) < F < 1. \quad (2.16)$$

The negative root in (2.15) must be chosen to ensure that energy propagation is upward-normal to the slope. The positive root, which has downward energy propagation, is disallowed by two constraints. For flow that satisfies (2.16) the positive-root group velocity has a component downward normal to the slope, so such waves may not be generated on the slope. For slower flow, with $F < \sin(a)$, the direction of energy propagation, while still downward, would be upward normal to the slope. However, in this regime m is imaginary, by (2.15), so no wave solutions exist. This result is consistent with the analysis of Thorpe (1992, 1996) in the case of corrugations that run directly downslope.

Returning to the solution of the wave problem, we may relate w and υ by combining the y- and z-momentum equations (2.1) as

$$w_{tty} + w_y N^2 = \upsilon_{ttz}. \quad (2.17)$$

Assuming a solution for υ of the form

$$\upsilon = \upsilon_o \sin[k(x - Ut) + m(z - \alpha y)], \quad (2.18)$$

we may solve (2.17) to find

$$\upsilon_o = w_o \alpha \left(\frac{1 - F^2}{F^2} \right). \quad (2.19)$$

Using this in the boundary condition equation (2.13) allows us to solve for w_o. Then u, p', and ρ' are readily found by straightforward manipulation. The full wave solution is

$$\frac{p'}{\rho_o} = U^2 k \delta_V G \sin(P)$$

$$\frac{g\rho'}{\rho_o} = N^2 \delta_V G^2 \left(\frac{F^2}{1 - F^2}\right) \cos(P), \qquad (2.20)$$

where

$$P = (kx + ly + mz - \sigma t)$$
$$= k(x - Ut) + m(z - \alpha y)$$
$$k = k, \quad l = -\alpha m = \alpha k G, \quad m = -kG, \quad \sigma = Uk$$

$$G = \left[\frac{1 - F^2}{F^2 - \alpha^2(1 - F^2)}\right]^{1/2}$$

$$F = \frac{Uk}{N}, \quad \text{and} \quad \sin(a) < F < 1. \qquad (2.21)$$

The function $G(F)$ is plotted in Fig. 2a ⬤ for several values of slope angle. As F decreases toward the low-speed cutoff, $\sin(a)$, G becomes very large, and with it all the terms in the wave solution (2.20).

b. Evanescent solutions

The complete solution requires evanescent flows, both slower than the low-speed cutoff and faster than the high-speed cutoff. To find these we return to the original form of the vertical velocity (2.7) and assume m is imaginary. The appropriate forms of w and υ to use in Eqs. (2.9) and (2.17) are

$$w = w_o \sin[k(x - Ut)] \exp[-kG'(z - \alpha y)]$$
$$\upsilon = \upsilon_o \sin[k(x - Ut)] \exp[-kG'(z - \alpha y)], \qquad (2.22)$$

where

$$G' = (-G^2)^{1/2}, \qquad (2.23)$$

and $G'(F)$ is plotted in Fig. 2a ⬤. These yield the same relation between υ_o and w_o as given by (2.19). Then the boundary condition equation may be solved, and the full solution derived as before. The full evanescent solution is found to be

$$\frac{g\rho'}{\rho_o} = N^2\delta_V G'^2\left(\frac{F^2}{1-F^2}\right)\cos[k(x-Ut)]$$

$$\times \exp[-kG'(z-\alpha y)] \qquad (2.24)$$

for $0 < F < \sin(a)$ or $F > 1$.

An important property of the wave and evanescent solutions is the nature of water parcel paths on the slope. This is because the path may indicate how the flow will respond to topographic variation that is larger than the linearized solution allows. If the parcel paths are mainly over the ridges (as in Fig. 1 ◯), then we expect the nonlinear flow to develop lee waves with possible wave breaking behind the ridge, as observed in many laboratory and atmospheric flows (Baines 1995) and in the ocean (Nash and Moum 2001). If, on the other hand, parcel paths go around the ridges following isobaths, then we expect horizontal flow separation, as in SG. The isobath aspect ratio, $k\delta_V/\alpha$, may easily be $O(1)$ on the sloping ocean margin, even though the vertical aspect ratio, $k\delta_V$, is small. It will be helpful to introduce the term $\delta_H = \delta_V/\alpha$, which is the cross-slope width of isobath variation for a topographic feature.

The orientation of a fluid parcel path on the slope may be defined by an angle, b, which is the angle of the plane of motion of fluid parcels (defined in the same manner as a), where

$$\tan(b) = \frac{w}{v} = \alpha\left[\frac{F^2}{\alpha^2(1-F^2)}\right]. \qquad (2.25)$$

The angle b is plotted versus F in Fig. 3a ◯ for $\alpha = 0.1$. The amplitude of the cross-slope flow v is plotted in Fig. 3b ◯. In that figure, v is normalized by v_{around}, the value it would have for purely horizontal flow (i.e., flow around the ridges and into the canyons with no vertical motion). Evanescent fast flow, with $F^2 \gg 1$, has $b = -\pi/2 + a$, which corresponds to potential flow over a path normal to the slope with no effect of buoyancy. As the flow slows to $F < 1$, waves are generated and parcel paths go mainly up and down with a tendency to move uphill on ridge crests, as shown by the upper dashed line in Fig. 1 ◯. As the flow slows and $F \rightarrow \sin(a)$, this tendency is increased: $b \rightarrow a$ and parcel paths go far up on ridge crests. As F passes through $\sin(a)$ into the low-speed evanescent solution, the cross-slope parcel motion is still large but the sense is reversed: parcel paths now swing far down the slope on ridge crests and move upslope in canyons. In the low-speed limit $b \rightarrow 0$ as $F \rightarrow 0$, which corresponds to purely horizontal flow around the ridges.

c. Limits of the linearized solutions

We now return to the question of the limits of consistency of the solutions. The fundamental linearization of the equations involved the assumption $\mathbf{u} \cdot \nabla(\ ) \ll \partial(\ )/\partial t$. From the wave solution (2.20), this constraint may be expressed as limits upon the corrugation steepness:

$$k\delta_V \ll \begin{cases} 1/G & \text{(from } u\partial/\partial x) \\ 1/(\alpha^2 G^3) & \text{(from } v\partial/\partial y) \\ (1-F^2)/(F^2 G^3) & \text{(from } w\partial/\partial z). \end{cases} \qquad (2.26)$$

The three sets of curves are plotted versus F in Fig. 3c ◯. For the wave solution the constraint from $w\partial/\partial z$ is always the strongest, and is most stringent near $F = \sin(a)$. For F and α both small (as is typical of many oceanic flows), the constraint from $w\partial/\partial z$ may be written approximately as

$$k\delta_V \ll (F^2-\alpha^2)^{3/2}/F^2, \qquad (2.27)$$

which increases approximately linearly with F near $F = \sin(a)$.

The derivations also assumed $u \ll U$ for the boundary condition, which gives rise to the same expression as found for $u\partial/\partial x$. An identical constraint results from our application of the boundary condition on $z = \alpha y$ instead of $z = \eta$.

The expressions derived from the evanescent solution are identical to (2.26), except that G' appears instead of G. For the low-speed evanescent solution, in the limit $F \to 0$, the constraint from either $u \partial/\partial x$ or $v \partial/\partial y$ becomes

$$k\delta_V \ll a, \quad (2.28)$$

which may also be written as $k\delta_H \ll 1$. For slow flow along topography with $O(1)$ isobath aspect ratio, the linear solution expressly violates the linearizing assumptions. Thus, our solution may serve as a guide on the way toward horizontal flow separation, but will certainly not get all the way there.

3. Form stress and isolated ridges

The form stress due to wave generation is given by alongslope integration of either the Reynolds stress,

$$\frac{\tau}{\rho_o} = \int_0^\infty \overline{u_t}^x \, d(z - \alpha y)$$

$$= \cos(a)\overline{uw}^x|_{z=\alpha y} - \sin(a)\overline{uv}^x|_{z=\alpha y}, \quad (3.1)$$

or the pressure–slope correlation,

$$\frac{\tau}{\rho_o} = \overline{\frac{-p'}{\rho_o}\eta_x^N}^x\bigg|_{z=\alpha y} = \cos(a)\overline{\frac{-p'}{\rho_o}\eta_x}^x\bigg|_{z=\alpha y}. \quad (3.2)$$

Here τ is the alongslope boundary stress per unit area on the slope (not the horizontal projected area). A positive stress accelerates the alongslope flow in the positive x direction, but only where the wave energy is absorbed. Thorpe (1996) suggests that this is likely on the shelf above the slope. In expressions (3.1) and (3.2), the overbar x denotes x averaging, and η^N is the slope elevation in the direction normal to the plane $z = \alpha y$. From either expression the normalized form stress is calculated to be

$$\frac{\tau}{\frac{1}{2}\rho_o N^2 \delta_V^2} = \cos(a)F^2 G, \quad (3.3)$$

which is plotted versus F in Fig. 2b ⊙. For small values of α (0.1 being a "steep" slope in the ocean) the boundary stress is much like the $\alpha = 0$ case, until we approach the low-speed cutoff. There the stress jumps to very high levels (and $m \to \infty$) in a process much like critical wave reflection (Eriksen 1982). Physically such high stress will not be realized, as turbulence will overtake the near-boundary flow.

A final extension of the wave solution that will be helpful when considering the generation of horizontal eddies is the case of an isolated ridge topography running down the slope. We use standard methods of Fourier superposition (e.g., Baines 1995) to calculate the drag on a Gaussian ridge. A ridge of shape

$$\eta_R = \delta_V \exp\left(\frac{-x^2}{L^2}\right) + \alpha y \quad (3.4)$$

has Fourier transform

$$\tilde{\eta}_R = \delta_V L\sqrt{\pi} \exp\left(\frac{-L^2 k^2}{4}\right). \quad (3.5)$$

The force per unit cross-slope width, F_D, is

$$F_D = \frac{?}{\pi} \int_{\sin(a)N/U} \cdots \eta_R \cdots \delta_V^2 \cdots dk, \qquad (3.6)$$

where τ is given by (3.3). Changing the variable of integration from k to F (but assuming we are holding U and N constant) we may rewrite (3.6) as

$$\frac{F_D}{\rho_o N U \delta_V^2} = \frac{1}{2} \cos(a) \left(\frac{LN}{U}\right)^2$$

$$\times \int_{\sin(a)}^{1} \exp\left[\frac{-1}{2} F^2 \left(\frac{LN}{U}\right)^2\right] F^2 G \, dF, \quad (3.7)$$

where we have used the same normalization as in Gill (1982, figure on p. 279). The actual integration of (3.7) is done numerically. For $a = 0$ the integration is straightforward because the τ versus F curve is well behaved over the whole range of F (Fig. 2b ⬤). However, when $a \neq 0$, the function G is unbounded at $F = \sin(a)$, which cannot be ignored since our Gaussian ridge will always have some amplitude at that wavenumber. The function is integrable, however, since near $F = \sin$ (a) one may make use of the analytical form, $\int (c^2 - x^2)^{-1/2} \, dx = \arcsin(x/c)$, noting that $\arcsin(1) = \pi/2$.

The form stress on the ridge may also be expressed as a drag coefficient based on the frontal area of the ridge (i.e., looking alongslope). The drag coefficient is then given by

$$C_{DP} = \frac{F_D}{\frac{1}{2}\rho_o U^2 \delta_V \cos(a)}$$

$$= \frac{\delta_V}{L}\left(\frac{LN}{U}\right)^3 \int_{\sin(a)}^{1} \exp\left[\frac{-1}{2} F^2 \left(\frac{LN}{U}\right)^2\right] F^2 G \, dF. \quad (3.8)$$

Both forms of ridge drag are plotted versus U/LN in Fig. 4 ⬤ for various values of the slope angle. The subscript P in C_{DP} is for pressure because that is the source of the drag, as opposed to a frictional boundary layer. For small slopes there is a range of U/LN between the low- and high-speed cutoffs over which the form stress increases linearly with flow speed. This is typical of drag due to wave generation and is present in the solution without a slope.

Form stress may also be the primary source of drag when flow separation occurs. From a long history of aeronautics experiments on flow around bluff bodies (e.g., Hoerner 1965) the approximate result is that for bodies with aspect ratio (width to length) of order 1 the drag coefficient based on frontal area is $C_D = O(1)$. This subject is discussed in more detail in section 4.

In Fig. 4a ⬤ the wave drag for all values of the slope angle decreases rapidly for $U/LN > 1$, which is the effect of the high-speed cutoff (i.e., $F > 1$ in the single-wavenumber case). The net drag on the ridge also decreases markedly as the slope angle increases. In fact, for reasonable upper ocean values of U/LN and a we may very well have negligible wave drag on the ridge because the ridge has little amplitude at "draggy" wavenumbers. For example, on a slope of $a = 1/20$ with $L = 1000$ m, $N = 10^{-2}$ s^{-1}, and $U = 0.5$ m s^{-1} ($U/LN = 1/20$) the flow has about the same wave drag as for a ridge on a flat plane, but as the flow slows to $U = 0.125$ m s^{-1} ($U/LN = 1/80$) the wave drag essentially vanishes because of the low-speed cutoff in the wave solution. The negligible wave drag on the ridge also indicates that the flow will mainly be around the ridge, instead of over it.

Across a wide range of slope angles, this low-speed cutoff occurs at approximately

$$\frac{U}{LN \, \sin(a)} = \frac{1}{2}, \qquad (3.9)$$

which is marked with stars on Fig. 4a ⊙. The form of (3.9) is anticipated from the low-speed cutoff of the single-wavenumber case, $F = \sin(a)$. Expression (3.9) is used in the next section to predict whether a given ridge will or will not generate lee waves.

We may compare expression (3.9) with a related Froude number often seen in discussions of stratified flow over rough terrain (Snyder 1985; Baines 1995) based on obstacle height:

$$F_V = \frac{U}{N\delta_V}. \qquad (3.10)$$

Laboratory studies (Snyder 1985; Baines 1995) show that for $F_V < 1$ some portion of the flow will lack the kinetic energy to rise over a bump of height δ_V and will, instead, go around it. This simple, powerful scaling results from integration of the Bernoulli function along a steady streamline and so is inherently related to nonlinear inertia effects. On the other hand, expression (3.9) was arrived at purely from linear wave theory. The two expressions are similar if the isobath aspect ratio is near 1, for which $L = \delta_H$ and $\delta_V = \delta_H\alpha$. For isobath aspect ratios much different from 1, the expressions are no longer similar, and Eq. (3.9) should apply more generally to flow along slopes.

4. Numerical experiments

We use the Hallberg Isopycnic Model (HIM: Hallberg and Rhines 1996) to simulate stratified flow along a slope with a ridge. The channel is reentrant in the x direction and has a vertical free-slip wall at the far side of the channel ($y = 10$ km). The model is hydrostatic (equivalent to $Uk \ll N$ in the analytical solution) and integrates the shallow-water equations in a number of overlain constant-density layers. A C grid is used in the horizontal, while the vertical discretization moves with density interfaces. Layers may freely intersect topographic slopes. The upper boundary is a free surface. We generally use a 10 km × 10 km domain, 200 m deep, with a planar slope of $\alpha = 1/20$ along the $y = 0$ wall. The horizontal resolution is 100 m, and the initial vertical spacing is 5 m (40 layers). The density step between layers gives an overall buoyancy frequency of $N = 10^{-2}$ s^{-1}, typical of the upper ocean.

One may compare the low-speed cutoff frequency, $N \sin(a)$, with the Coriolis frequency, f, and with the intrinsic frequency of the flow, Uk. For an isolated ridge the highest wavenumber with significant variance is $k = 2/L$, so the analogous intrinsic frequency for the ridge is $2U/L$. In our runs $N \sin(a) = 5 \times 10^{-4}$ s^{-1}, while a typical value of f is 10^{-4} s^{-1}. Our slow-speed simulation has $2U/L = 2.5 \times 10^{-4}$ s^{-1}, 2.5 times f, and half of $N \sin(a)$. Based on this we neglect earth rotation. But one should be aware that slower, less stratified flow on more gradual slopes, or with broader ridges, will likely be affected by rotation, including boundary layer asymmetry (Trowbridge and Lentz 1991; MacCready and Rhines 1993; Garrett 1995).

The ratio of vertical to horizontal resolution is equal to the slope angle, so dynamical features that are inclined at that angle (such as the bottom boundary layer or a shed eddy) are equally well resolved in the vertical and horizontal. There are three primary dissipative terms in the momentum and layer thickness equations. A quadratic bottom drag with $C_{\mathrm{DBBL}} = 2.5 \times 10^{-3}$ slows flow in the bottom boundary layer. The bottom boundary layer thickness is dynamically determined as a function of shear and stratification (Killworth and Edwards 1999) and is 15–25 m on the slope. The horizontal thickness of the boundary layer is 20 times this, ~ 400 m, because it lies on the slope. A biharmonic lateral diffusion, with coefficient $A_H = 6 \times 10^4$ m^4 s^{-1}, damps out velocity gradients near the grid scale. Momentum and thickness are mixed between layers according to diffusivities that are a function of the local gradient Richardson number. Background levels of vertical eddy viscosity and diffusivity are set at 10^{-4} m^2 s^{-1}. These background levels have a negligible effect upon the overall flow evolution.

Figure 5 ⊙ shows results of the model for a test of the linear analytical solution. The channel topography is a single cosine corrugation on the slope, with wavelength of 2 km and vertical amplitude 0.318 m. Flow is accelerated smoothly in the alongchannel direction, using half of a sine function, over 1.5 h, until $U = -0.191$ m s^{-1}. For these parameters $F = Uk/N = 0.06$, slightly greater than $\sin(a) = 0.05$, so wave generation is expected, and the predicted vertical amplitude of interface displacement is 1 m. Unlike most of the simulations, this run was designed to test the linear theory, and had no mixing or bottom friction and extremely small interfacial friction. After 6 h, the phase lines of interface displacement tilt into the flow, close to the predicted angle. However, the interfaces are displaced upward at the ridge with only 60% of the predicted amplitude, possibly because the flow is not completely inviscid (the horizontal biharmonic diffusion is still active). The amplitude of $k\delta_V$ is about 10% of the critical value for formal consistency of the linear solution, so we expect to be in the linear regime.

Next, a series of numerical experiments was performed using an isolated Gaussian ridge on the slope at midchannel. The vertical height of the ridge, δ_V, was varied from 1 to 100 m, and the alongchannel length scale of the ridge was $L = 1000$ m. The cases with a 1-m ridge were essentially inviscid, as in the cosine run in Fig. 5 ⚬. All the other runs had the more realistic levels of diffusivity and bottom drag described above. Because the slope angle is shallow, the isobath excursions, δ_H/L, are $O(1)$ for the larger ridges, even though the alongchannel steepness on the ridge flank, δ_V/L, is always much less than one. For each ridge height two experiments were performed, one with alongchannel velocity $U = -0.5$ m s^{-1} ($U/LN = 1/20$) and one with $U = -0.125$ m s^{-1} ($U/LN = 1/80$). For this slope angle the faster flow is well within the wave-generating regime, while the slower flow is not, being below the low-speed cutoff for this ridge, as predicted in Fig. 4 ⚬. The alongchannel flow is created by a body force applied over the first 1.5 h in such a way as to accelerate the fluid smoothly during that time, minimizing initial transients. Results from the two different cases are generally presented at either 3 h (fast flow) or 12.5 h (slow flow) after this initial adjustment. The approximate factor of 4 difference is meant to account for the different advective speeds. In both cases the fluid will have moved about 5.5 km in the alongchannel direction: long enough to set up the ridge wake, but not so long that the results will be much contaminated by the reentrant setup of the channel. The simulations included a tracer field, initialized as stripes in the alongchannel direction in each layer, in order to visualize the cross-channel stirring process.

In the fast-flow case over the 60-m ridge (Fig. 6b ⚬), lee wave generation is quite evident in the interface displacement. Much of the pattern is essentially stationary, especially the upward displacement on the front of the ridge and the large undulations in the lee. These are the parts that contribute to the form stress on the ridge. The typical lee wave wavelength is expected to be about $2(2)^{1/2}\pi U/N \cong 440$ m, somewhat shorter than the ridge. Based on studies of stratified flow over ridges (Snyder 1985), we expect flow separation in the vertical plane to occur in the first lee trough, as observed in Fig. 6b ⚬, although there is significant horizontal velocity as well. Comparing this with the slow-flow case (Fig. 6c ⚬) over the same ridge, the main difference is the almost complete lack of interface displacement. This is consistent with the predicted lack of wave drag in this case.

Looking at a middepth layer for these two simulations we see differences in the horizontal flow as well. The shape of a layer interface for the fast-flow case is plotted in Fig. 7a ⚬, showing a pattern combining both a lee wave and horizontal flow separation. Klymak and Gregg (2001) observe roughly comparable flow features in stratified tidal flow through a sill/constriction in a fjord. The vertical component of relative vorticity in this layer is plotted in Fig. 7b ⚬. The relative vorticity, ζ, has been normalized by $\zeta_o \equiv |-U/\delta_H|$, the expected scale of wake vorticity for fully separated flow. Another way to scale the vorticity would have been to use the horizontal width of the boundary layer, $W_{BBL} = H_{BBL}/\alpha$, instead of δ_H. This would be appropriate for the vorticity in the sloping boundary layer in the absence of flow separation. Only positive values of ζ/ζ_o are contoured, with contour intervals of 0.5 starting at 0.5. A small area of strong scaled vorticity is evident in the boundary layer at the crest of the ridge in Fig. 7b ⚬, and there is a patchy vorticity anomaly in the wake with maximum scaled value just over 2. The tracer field (Fig. 7c ⚬) shows the large-scale distortion of flow around the ridge. The tracer has very small concentration in the lee of the ridge because it has been mixed away vertically into neighboring layers.

Examining the same fields for the slow-flow simulation on the same ridge, there are several striking differences. The layer shows little vertical displacement (Fig. 8a ⚬); however, it develops a strong horizontal eddy in the wake of the ridge (Fig. 8b ⚬) with scaled vorticity greater than 4. The pattern of wake vorticity is essentially the same as observed in SG, as is its formation process: advection of boundary layer vorticity into the interior by horizontal flow separation at the ridge crest and subsequent horizontal diffusion of the vorticity filament over the wake region. The effect of the eddy is evident in the spiraling tracer field (Fig. 8c ⚬), which is not dissipated because there is little diapycnal mixing in this case.

The horizontal flow separation in these two cases is an extremely important property if we wish to understand the potential for exchange of boundary layer and interior fluid. In the slow-flow (evanescent) case we fully expect that the flow will separate at or near the ridge crest, as observed. Classic analyses of flow around a bluff body (e.g., Kundu 1990, 317–327) with steady laminar flow and zero large-scale pressure gradient show that reversal of the alongstream pressure gradient due to nonlinear terms near the body will in most cases reverse (and hence cause separation of) flow that has already been slowed by friction near the boundary. Over a very large range of "subcritical" Reynolds numbers, Re = 50 to 10^5, flow past a circular cylinder develops steady or periodically shedding vortices similar in size to the cylinder diameter (Hoerner 1965; van Dyke 1982; Kundu 1990). In geophysical flows (Wolanski et al. 1984; SG) the effective Reynolds number of tidal flow past islands and headlands (particularly those of scale comparable to the tidal excursion) is often in this range because the lateral eddy viscosity tends to be much larger than the kinematic molecular viscosity (by about six orders of magnitude). In our simulations we use a biharmonic lateral diffusivity for momentum, A_H, and the analogous Reynolds number is Re = UL^3/A_H, where L is a horizontal length scale of the ridge. For our slow-flow simulations Re = 1.6×10^4, well within the subcritical regime.

Signell and Geyer analyzed flow separation for the case of shallow tidal flow around a coastal headland. Here, two additional factors beyond those of classic cylinder flow become important. First, if the alongshore flow is highly damped by bottom friction, then there can be a large-scale pressure gradient required to create the alongcoast flow (Wolanski et al. 1984). This pressure gradient can, in principle, overwhelm the adverse pressure gradient due to advection near the headland, thereby avoiding flow separation. On the other hand, if bottom friction is unimportant but there is a temporally reversing large-scale pressure gradient driving the tidal current, then there will always be a significant part of the tidal period when the pressure gradient is adverse (Black and Gay 1987). However, in this case, the pressure gradient is still almost always of the same sign along the boundary, so again flow separation may not occur. Signell and Geyer found that for salient headlands with "typical" coastal water depth and tidal period that the advection terms usually dominated, causing flow separation near the point of the headland. Our evanescent simulations are solidly in the separating regime because they have no large-scale, alongcoast pressure gradient. Also, because our simulations are ten times as deep as those in SG, the frictional effects are reduced by that factor. In this respect, our simulations are like a realistic version of the low-bottom-friction cases considered by SG.

In the case of our wave-generating simulations the situation is more complicated. The flow tends, at least on the front of the ridge, to follow a path over the ridge instead of around it (Fig. 7 ⊙). This weakens the advection terms that cause the adverse pressure gradient. However, in the lee of the ridge there are large pressure reversals due to the lee wave, and it is apparent that flow separation, and some injection of boundary layer fluid, also occur in this case, although somewhat downstream of the ridge crest.

a. Form stress in the numerical simulations

A primary goal of understanding stratified flow along rough slopes is to be able to predict the rate at which fluid near the slope may be exchanged with the interior through stirring by horizontal eddies. In this paper we are exploring some of the basic dynamics upon which a more general theory of "coastal stirring" could be based. One simple scaling that we may make relating to coastal stirring is of the maximum offshore transport that may be caused by flow past an isolated obstacle. For a ridge with projected frontal area $H\delta_H$, facing an alongslope flow of scale U, the maximum offshore volume transport will be

$$T_{max} = UH\delta_H. \quad (4.1)$$

Two major assumptions go into (4.1): First, that all the fluid redirected by the ridge is pushed out away from the boundary layer. This is clearly true for the horizontal separation in Fig. 8 ⊙, but is not true for the simple case of frictional slowing in a bottom boundary layer without separation: there the slowed fluid remains on the slope. The second assumption in (4.1) is that all the fluid encountered by the ridge is slowed to zero alongslope momentum. Equivalently we could say that the ridge has a drag coefficient of 1 based on its projected frontal area. The first assumption depends upon what happens to the slowed fluid in the wake, and we do not address it in this paper. We will, however, make drag calculations, to see if the second assumption is warranted. We do this by calculating the form stress on the ridge. The total drag on the boundary includes the tangential boundary layer stress, which does not necessarily contribute to horizontal stirring. The form stress may have two sources: internal wave generation and horizontal flow separation. The fluid slowed by wave drag may be in the lee of the ridge if there is wave dissipation there (as is the case in our simulations) or quite distant if the energy propagates. The fluid slowed by flow separation is directly in the lee of the ridge and is advected slowly downstream (self-advection of the wake vortex tends to keep the eddy near the ridge).

We cannot, in principle, separate wave drag from separation drag because both are kinds of form stress. We proceed by calculating the form stress in the numerical simulations, assuming, based on the linear solution illustrated in Fig. 4 ⊙, that it will be due mainly to waves in the fast-flow cases, and mostly due to separation in the slow-flow cases.

The form stress on the slope is calculated as the bottom pressure multiplied by the alongchannel slope angle, integrated over the entire domain. This is plotted for one of the wave-regime runs in Fig. 9 ⊙. The net form stress increases over the first 1.5-h acceleration time, and then decays slowly. During the latter part of the run we may calculate a drag coefficient based on the projected frontal area of the ridge and the nominal (constant) alongslope velocity, as is shown in Fig. 9b ⊙. The mean drag coefficients, averaged over the last half of each run, are plotted in Fig. 10 ⊙. Because the drag is not constant in time, the averaged drag coefficients should be considered as rough estimates, good to approximately ±50%. Also plotted in Fig. 10 ⊙ is the predicted drag coefficient for the wave-generating case from (3.8). Several trends are apparent. Large ridges have much more drag because of increased frontal area and larger drag coefficients. While the predicted drag coefficient from linear theory grows linearly with ridge height, the drag coefficients from the numerical simulations in the wave regime drop off for larger ridges, approaching $C_{DP} \approx 1.2$. The inability of the large ridges to support the large

predicted drag values is presumably due to dissipation in the lee wave, which limits wave growth and hence the pressure drop across the ridge. In addition, the horizontal boundaries at the free surface and flat bottom limit vertical motion in those places. While such boundaries are a natural part of oceanic flow, and are required for a finite numerical domain, they make the numerical setup different from the analytical problem, which had a slope of infinite extent. In the evanescent regime

there is little vertical motion, so we expect the horizontal boundaries to have only a minor effect. However, examination of the bottom pressure field shows a tendency for drag on the lower half of the ridge to be greater than that on the upper half, varying by up to ±50% about the mean for the larger ridges and even more for the smaller ridges. This tendency may result from more rapid slowing of the flow over shallower topography and from wave reflection off the free surface. This effect, as well as the time dependence mentioned above, reinforces the conclusion that the calculated drag coefficients are only rough estimates and could be somewhat larger if a deeper channel were used.

The mean drag coefficient from the evanescent-regime numerical runs (Fig. 10 ⊙) is surprisingly similar to the wave-regime cases, although about 20% smaller in size. The actual drag on the ridge for the evanescent cases is about 1/20 of that for the wave cases since the alongchannel flow is ¼ as big. Again, the form stress grows approximately linearly with ridge height, and then levels off, this time at $C_{DP} \approx 1$. The linear increase of drag coefficient with isobath aspect ratio is consistent with results from experiments on elliptical cylinders. For cylinders of aspect ratio (alongflow length/cross-flow length) in the range from 0.1 to 1, the drag coefficient based on frontal area varies approximately as $C_D = 1.1 \times$ (cylinder aspect ratio) for subcritical Reynolds number (Hoerner 1965). The form stress is the direct result of the flow separation in this case since fluid in the wake eddy has experienced a loss of Bernoulli function through diffusion of the vorticity from the separated boundary layer. While the actual drag on the ridge is much larger for the wave-generating case than for the evanescent case, they both appear to have involved about the same volume of fluid in the vortical wake eddy. Because we are looking at the two runs at different times, when about the same amount of fluid has advected past the ridge, we may conclude that in both cases there is the potential for a significant amount of fluid exchange between boundary layer and interior.

The sensitivity of the form stress to choice of C_{DBBL} was explored in four supplementary simulations using the ridge with $\delta_V = 60$ m. In both wave-generating and evanescent regimes, C_{DBBL} was varied by a factor of 20 from 5×10^{-4} to 10^{-2}. The calculated pressure drag coefficient in the wave-generating regime varied from 1.26 to 0.76. The larger pressure drag associated with lower C_{DBBL} is presumably due to decreased damping of lee waves. In the evanescent regime, C_{DP} showed much less sensitivity, varying only from 0.85 to 0.83. In all cases the qualitative flow features, such as lee wave and separation patterns, were unchanged.

The results of the form stress analysis indicate that in both cases the drag coefficient C_{DP} becomes $O(1)$ when the ridge horizontal aspect ratio, δ_H/L becomes $O(1)$ or greater (e.g., for $\delta_V = 60$ m and $\alpha = 1/20$, $\delta_H/L = 1.2$).

b. Energetics in the numerical simulations

Another way of looking at the numerical experiments is to consider the overall energetics. In Fig. 11 ⊙ the volume-integrated kinetic and potential energies are plotted versus time for the wave-regime run with the 60-m ridge. The KE is calculated in the frame of reference moving with the constant nominal offshore velocity ($U = -0.5$ m s^{-1} in this case). Thus, the KE represents just the perturbation energy associated with the boundary layer and interior wave and eddy responses. The energy grows with time as the boundary layer (which accounts for nearly half of the KE) and interior response grow. The available potential energy (APE) is calculated at each time step as the potential energy above that of the resting state of the interfaces at that time step. We must use a different base state at each time step because mixing permanently increases the base-state potential energy over time. The PE of this base state is also plotted in Fig. 11 ⊙ (where it is assumed that the base-state PE is zero at the beginning of the run). The change in base-state PE is about the same in all the wave-regime runs with mixing, varying from 2.5×10^4 to 3.5×10^4 J as the ridge height goes from 20 to 100 m. This implies that most of mixing occurs in the boundary layer. As we see below, these runs develop a bottom mixed layer, although it is modified by both the slope and the ridge wake. As the ridge height increases the APE grows in amplitude along with the lee wave, as one would expect. The ratio of APE/(APE + KE) is also plotted in Fig. 11 ⊙. The time average of this energy ratio over the last half of each run is plotted versus ridge height in Fig. 12 ⊙. For the 1-m ridge (which is a nearly inviscid run) in the wave regime the energy ratio is close to 0.5, which is expected from linear theory for nonrotating internal gravity waves. The energy ratio drops markedly for all cases when realistic dissipation is included (as it is for all the runs with larger ridges). The increased importance of KE is due to the boundary layer, the finite channel depth, and the formation of wake vorticity. The energy ratio for all the evanescent-regime runs is much smaller than that of the wave-regime runs, which is expected because of the lack of significant wave activity.

Cross-channel sections of interface depth for one of the wave-regime runs ($\delta_V = 60$ m) are shown in Fig. 13 ⊙. In Fig. 13b ⊙ the section is taken upstream of the ridge and represents the flow nearly undisturbed by the ridge. Here the formation of a bottom mixed layer is apparent on both the slope and the flat bottom, although this layer is markedly thinner on the slope. This may be evidence of a competition between shear-induced mixing and the lateral restratification caused by the slumping of tilted isopycnals. Downstream of the ridge (Fig. 13c ⊙) in the middle of the wake eddy/lee wave, the picture is much more complicated. Here the thick bottom mixed layer is still present on the flat bottom, but over most of the

slope layer interfaces show evidence of significant restratification. This may be because the currents are weak near the slope on this section due to the flow modification from the ridge. Offshore in Fig. 13c ⊙ there are at least two other regions of prominent thickening of layers. The outermost may be traced to the lee wave of the ridge. The middle one is caused by separation of the boundary layer sending mixed fluid into the interior in the wake eddy. This complex interplay of wake and boundary layer effects makes the quantification of boundary layer–interior exchange in the wave regime a key topic for future work.

5. Summary and conclusions

In this paper we have explored wave and eddy generation by stratified flow along a slope with a ridge. The inquiry is motivated by the complex bathymetry, particularly the prominent corrugations, of the continental margin, and by a need to understand the scales and mechanisms of coastal stirring, important to biological and pollutant dispersal and to the mixing of ocean stratification. The original analytical, single-wavenumber theory due to Thorpe (1992, 1996) has been extended to include evanescent regimes and the case of an isolated Gaussian ridge. The flow possesses an interesting "low speed cutoff" to wave generation, occurring when the frequency of fluid parcels encountering ridge crests is equal to $N \sin(a)$. Only for flow below this speed do fluid parcels tend to flow along isobaths, going around ridges instead of over them. For the case of an isolated ridge these regimes also exist, with large form stress predicted for flow in the wave-generating regime.

The solutions were extended beyond the linear approximation using 3D numerical simulations with an isopycnic numerical model. Nonlinearity causes the development of diapycnal mixing in the wake of the ridge for flow in the wave regime, whereas horizontal separation at the ridge crest is the prominent feature of flow in the evanescent regime. The pressure drag coefficient, based on the projected frontal area of the ridge, was calculated and found to increase linearly with the isobath aspect ratio of the ridge, $\delta_H/L,$ reaching $C_{DP} \approx 1$ to 1.2 where $\delta_H/L = 1$ and thereafter leveling off. The order-one drag coefficient suggests that we may scale the maximum rate of volume exchange between the slope and the interior as $U\delta_H H$. Whether or not this maximum transport is achieved depends upon whether the slowed fluid is pushed offshore. Tidal oscillation of the driving alongshore current occurs in most places on the continental margin, so consideration of the interaction of successive ridge drag events of opposite sign will be important for realistic prediction and parameterization of coastal stirring.

REFERENCES

Allen S. E., 2000: On subinertial flow in submarine canyons: Effect of geometry. *J. Geophys. Res*, **105**, 1285–1298. Find this article online

Alvarez A., J. Tintore, and A. Sabates, 1996: Flow modification and shelf-slope exchange induced by a submarine canyon off the northeast Spanish coast. *J. Geophys. Res*, **101**, 12043–12055. Find this article online

Armi L., 1979: Effects of variation in eddy diffusivity on property distributions in the oceans. *J. Mar. Res*, **37**, 515–530. Find this article online

Baines P. G., 1995: *Topographic Effects in Stratified Flows*. Cambridge University Press, 482 pp.

Black K. P., and S. L. Gay, 1987: Eddy formation in unsteady flows. *J. Geophys. Res*, **92**, 9514–9522. Find this article online

Boyer D. L., and X. Zhang, 1990: Motion of oscillatory currents past isolated topography. *J. Phys. Oceanogr*, **20**, 1425–1448. Find this article online

Cannon G. A., and D. E. Bretschineder, 1986: Interchanges between coastal and fjord circulation. *Rapp. P.-v. Reun. Cons. Int. Explor. Mer*, **186**, 38–48. Find this article online

Chapman D. C., and G. Gawarkiewicz, 1995: Offshore transport of dense shelf water in the presence of a submarine canyon. *J. Geophys. Res*, **100**, 13373–13387. Find this article online

Codiga D. L., 1993: Laboratory realizations of stratified seamount-trapped waves. *J. Phys. Oceanogr*, **23**, 2053–2071. Find this article online

Codiga D. L., 1997: Observations of low-frequency circulation and amplified subinertial tidal currents at Cobb seamount. *J. Geophys. Res*, **102**, 22993–23007. Find this article online

Codiga D. L., D. P. Renouard, and A. M. Fincham, 1999: Experiments on waves trapped over the continental slope and shelf in a continuously stratified rotating ocean, and their incidence on a canyon. *J. Mar. Res*, **57**, 585–612. Find this article online

Eriksen C. C., 1982: Observations of internal wave reflection off sloping bottoms. *J. Geophys. Res*, **87**, 525–538. Find this article online

Garrett C., 1995: Flow separation in the ocean. *Topographic Interactions in the Ocean: Proc. 'Aha Huliko'a Workshop,* Honolulu, HI, Hawaii Institute of Geophysics, 119–124.

Garrett C., P. MacCready, and P. B. Rhines, 1993: Boundary mixing and arrested Ekman layers: Rotating, stratified flow near a sloping boundary. *Annu. Rev. Fluid Mech*, **25**, 291–323. Find this article online

Gill A. E., 1992: *Atmosphere–Ocean Dynamics*. Academic Press, 662 pp.

Hallberg R., and P. B. Rhines, 1996: Buoyancy-driven circulation in an ocean basin with isopycnals intersecting the sloping boundary. *J. Phys. Oceanogr*, **26**, 913–940. Find this article online

Hickey B. M., 1998: Coastal oceanography of western North America from the tip of Baja California to Vancouver Island. Chapter 12 of *The Sea.* Vol. 11, A. R. Robinson and K. H. Brink, Eds., John Wiley and Sons, 345–393.

Hoerner S. F., 1965: *Fluid-Dynamic Drag,.* Hoerner Fluid Dynamics.

Killworth P. D., and N. R. Edwards, 1999: A turbulent bottom boundary layer code for use in numerical ocean models. *J. Phys. Oceanogr*, **29**, 1221–1238. Find this article online

Klymak J. M., and M. C. Gregg, 2001: The three-dimensional nature of flow near a sill. *J. Geophys. Res.*, in press.

Kundu P. K., 1990: *Fluid Mechanics*. Academic Press, 628 pp.

Kunze E., and T. B. Sanford, 1993: Submesoscale dynamics near a seamount. Part I: Measurements of Ertel vorticity. *J. Phys. Oceanogr*, **23**, 2567–2588. Find this article online

Lentz S. J., and J. H. Trowbridge, 1991: The bottom boundary layer over the northern California shelf. *J. Phys. Oceanogr*, **21**, 1186–1201. Find this article online

Lighthill J., 1978: *Waves in Fluids*. Cambridge University Press, 504 pp.

MacCready P., and P. B. Rhines, 1991: Buoyant inhibition of Ekman transport on a slope and its effect on stratified spin-up. *J. Fluid Mech*, **223**, 631–661. Find this article online

MacCready P., and P. B. Rhines, 1993: Slippery bottom boundary layers on a slope. *J. Phys. Oceanogr*, **23**, 5–22. Find this article online

Nash J. D., and J. M. Moum, 2001: Internal hydraulic flows on the continental shelf: High drag states over a small bank. *J. Geophys. Res*, **106**, 4593–4612. Find this article online

Ott M. W., and C. Garrett, 1998: Frictional estuarine flow in Juan de Fuca Strait, with implications for secondary circulation. *J. Geophys. Res*, **103**, 15657–15666. Find this article online

Petruncio E. T., L. K. Rosenfeld, and J. D. Paduan, 1998: Observations of the internal tide in Monterey Canyon. *J. Phys. Oceanogr*, **28**, 1873–1903. Find this article online

Pratson L. F., and W. F. Haxby, 1996: What is the slope of the U.S. continental slope? *Geology*, **24**, 3–6. Find this article online

Robinson I. S., 1993: Tidally induced residual flows. *Physical Oceanography of Coastal and Shelf Seas,* B. Johns, Ed., Elsevier Science, 321–356.

Roden G. I., and B. A. Taft, 1985: Effect to the Emperor Seamounts on the mesoscale thermohaline structure during the summer of 1982. *J. Geophys. Res*, **90**, 839–855. Find this article online

Signell R. P., and W. R. Geyer, 1991: Transient eddy formation around headlands. *J. Geophys. Res*, **96**, 2561–2575. Find this article online

Smith L. T., 1992: Numerical simulations of stratified rotating flow over finite amplitude topography. *J. Phys. Oceanogr*, **22**, 686–696. Find this article online

Snyder W. H., 1985: Fluid modeling of pollutant transport and diffusion in stably stratified flows over complex terrain. *Annu. Rev. Fluid*

Mech, **17**, 239–266. Find this article online

Thorpe S. A., 1992: The generation of internal waves by flow over the rough topography of a continental slope. *Proc. Roy. Soc. London A*, **439**, 115–130. Find this article online

Thorpe S. A., 1996: The cross-slope transport of momentum by internal waves generated by alongshore currents over topography. *J. Phys. Oceanogr*, **26**, 191–204. Find this article online

Torgrimson G. M., and B. M. Hickey, 1979: Barotropic and baroclinic tides over the continental slope and shelf off Oregon. *J. Phys. Oceanogr*, **9**, 945–961. Find this article online

Trowbridge J. H., and S. J. Lentz, 1991: Asymmetric behavior of an oceanic boundary layer above a sloping bottom. *J. Phys. Oceanogr*, **21**, 1171–1185. Find this article online

van Dyke M., 1982: *An Album of Fluid Motion*. Parabolic Press, 176 pp.

White M., 1994: Tidal and subtidal variability in the sloping benthic boundary layer. *J. Geophys. Res*, **99**, 7851–7864. Find this article online

Wolanski E., J. Imberger, and M. L. Heron, 1984: Island wakes in shallow coastal waters. *J. Geophys. Res*, **89**, 10553–10569. Find this article online

---

Figures
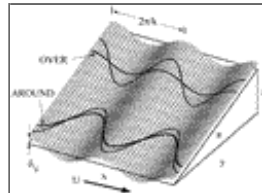
Click on thumbnail for full-sized image.

FIG. 1. Corrugated slope definition sketch. Two sets of possible streamlines are shown. The set labeled "OVER" is typical of solutions with wave generation: parcels pass up over ridges and down in the canyons. The solid line is a path with constant y. The streamlines labeled "AROUND" are typical of the low-speed evanescent solutions. Here the solid line is a path at constant z.
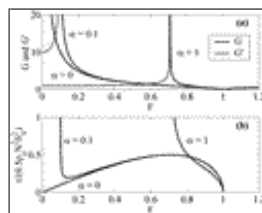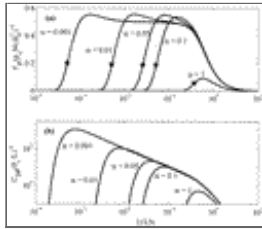

Click on thumbnail for full-sized image.

FIG. 2. (a) The function $G(F)$ from the corrugated slope wave solution plotted as solid lines for three slope angles α. Also plotted as dashed lines, for the two cases with nonzero slope, is the function $G'(F)$ from the evanescent solution. The function amplitudes increase rapidly near the low speed cutoff at $F = \sin(a)$. For $\alpha = 0.1$, $\sin(a) = 0.1$, while for $\alpha = 1$, $\sin(a) = 0.7$. (b) The normalized form stress (3.3) versus F plotted for the same three slope angles. Note that there is no form stress either below the low-speed cutoff or above the high-speed cutoff
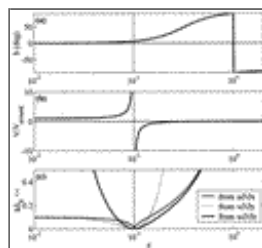
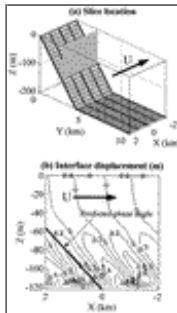Click on thumbnail for full-sized image.

FIG. 3. (a) The angle $b(F)$ from equation (2.25) is plotted for a slope $\alpha = 1/10$. This is the angle from the horizontal of the plane on which fluid parcel trajectories lie. Hence, very slow flow has $b = 0°$, while flow with F near $\sin(a)$ has $b = a$. For very fast flow the plane of parcel motion is normal to the slope. (b) The magnitude of the cross-slope flow, normalized by the value it would

have for motion on a horizontal plane (purely "AROUND"). The cross-slope velocity is very large near $F = \sin(a)$, and changes sign there. (c) The curves defining the formal limits of consistency of the linear solutions plotted for the case of slope $\alpha = 1/10$. A linear approximation should be consistent if the corrugation slope angle $k\delta_V$ is much less than all three curves, for a given F. The nonlinear terms that give rise to each curve are shown in the legend
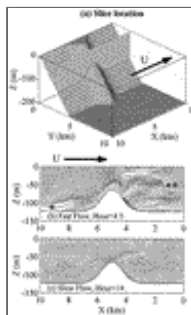

Click on thumbnail for full-sized image.

FIG. 4. (a) The normalized form stress per unit width across the slope due to a Gaussian ridge of width L is plotted vs U/LN for a variety of slope angles. In all cases the form stress drops off for $U/LN > 1$, which corresponds to flow faster than the high-speed cutoff. On the slower side, the form stress drops off near $U/(LN \sin a) = 1/2$, which is plotted with a star on each curve. This limiting value corresponds to flow near the low-speed cutoff. As the slope angle increases the region of U/LN with high form stress becomes more and more limited

Click on thumbnail for full-sized image.

FIG. 5. Numerical model results for the case of a slope with very small amplitude cosine corrugations. The topography is shown in (a); solid thick lines are drawn at ridge crests and dashed thick lines at troughs. Interface displacement (m) is contoured in (b). The predicted amplitude of the displacement is 1 m, while the observed amplitude is about 0.6 m. The predicated angle of phase planes is drawn as a thick line in (b). Interfaces are displaced upward at ridge crests, and the amount of displacement is twice δ_V, indicative of "more over" parcel paths (like the upper dashed line in Fig. 1)
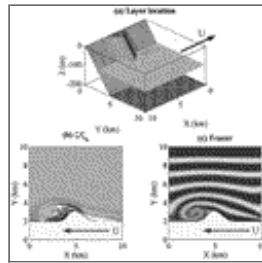

Click on thumbnail for full-sized image.

FIG. 6. Numerical model results for the case of a large Gaussian ridge ($\delta_V = 60$ m, $L = 1$ km, and $\alpha = 1/20$). Interface elevation is plotted on a section for two runs with different alongslope velocities. In (b) $U = -0.5$ m s^{-1}, and strong lee waves are generated. There is also a transient disturbance (**) heading downstream, and a bottom mixed layer (*) is evident in the increased layer thickness near the slope. In (c) $U = -0.125$ m s^{-1}, which is below the low-speed cutoff for wave generation, and interface displacement is slight

FIG. 7. Numerical model results for fast (wave regime, $U = -0.5$ m s^{-1}) flow past a ridge, as in Fig. 6b ⊙. (a) Upper interface elevation for a middepth layer is plotted, showing the lee-wave spatial structure. (b) Nondimensional relative vorticity in the layer. Positive values are contoured, with a contour interval of 0.5, starting at 0.5. (c) Tracer in the layer. The tracer concentration becomes small (less than 6% of its original value) in the lee due to diapycnal mixing. The flow goes up over the ridge, and then tends to separate horizontally about halfway down the lee side, giving rise to the distorted contact line on the slope between $y = 2$ and 3 km

FIG. 8. Numerical model results for slow (evanescent regime, $U = -0.125$ m s^{-1}) flow past a ridge, as in Fig. 6c ⊙. (a) Upper interface elevation for a middepth layer. (b) Nondimensional relative vorticity in the layer is plotted, showing a strong, coherent lee eddy. Positive values are contoured, with a contour interval of 0.5, starting at 0.5. (c) Tracer in the layer
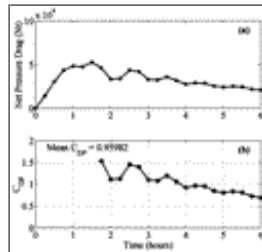
FIG. 9. Topographic form stress (a) exerted by the ridge on the flow versus time, for the wave-generating case, Fig. 6b ⊙. This drag can be due to both wave generation and flow separation, but does not include the frictional stress of the boundary layer. The drag grows during the initial 1.5 h, and then decays slowly. During the latter part of the run a drag coefficient (b) may be calculated, based on the projected frontal area of the ridge and the nominal flow speed (here $U = -0.5$ m s^{-1}). The mean value of the drag coefficient, averaged over the last half of the run, is shown in (b)
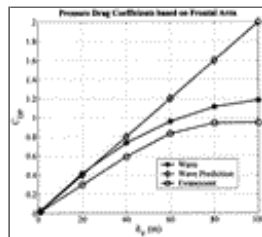
FIG. 10. Mean drag coefficients (see Fig. 9b ⊙) for all the single-ridge numerical simulations, plotted vs vertical ridge height. For ridge heights greater than about 50 m the isobath aspect ratio is greater than order one. Experiments in the wave-generating regime are plotted with stars, while those in the evanescent regime are plotted with circles. The analytical prediction of the drag coefficient [Eq. (3.8) applies only to the wave-generating regime) is plotted with diamonds. Ridges in both regimes can have large drag coefficients, leveling off to about $C_{DP} = 1$ as the ridge size increases. The wave-generating case matches the prediction well for small ridges
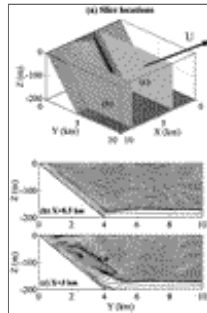
Click on thumbnail for full-sized image.

FIG. 11. Energies vs time for the single-ridge simulation of Fig. 6b ⊖▬ (wave-generating regime). (a) Perturbation kinetic energy for the whole domain. (b) Available potential energy. Since there is diapycnal mixing during the run, the basic stratification changes with time, as indicated by the "Base PE change" curve. (c) The ratio of APE to total perturbation energy
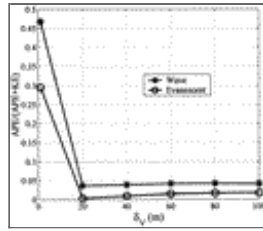
Click on thumbnail for full-sized image.

FIG. 12. Energy ratio for all the single-ridge numerical simulations. Two series of experiments were run, using different alongchannel velocities to put them in either wave-generating or evanescent regimes. The smallest ridge ($\delta_V = 1$ m) in the wave regime gives rise to an energy ratio near 0.5, as predicted by linear theory for nonrotating internal waves. The evanescent-regime runs always have a smaller fraction of potential energy. Finite amplitude ridges are also generally dominated by kinetic energy, due to the effects of dissipation, flow separation, and finite channel depth

Click on thumbnail for full-sized image.

FIG. 13. Sections of interface elevation across the channel for a run in the wave-generating regime (see Fig. 6b ⊖▬). Section (b) is in the region upstream of the ridge, and is at this time relatively unaffected by the flow perturbations from the ridge. The formation of mixed layers on the flat bottom and on the slope is apparent, although those on the slope are thinner. Section (c) is in the region just downstream of the ridge, and shows some of the effects of the ridge. The boundary layer on the slope is thinner, perhaps due to restratification. Just off the slope there is a thick region (*) due to boundary layer separation. Offshore of that a second thick region (**) is part of the lee wave structure

Corresponding author address: Parker MacCready, School of Oceanography, University of Washington, Box 355351, Seattle, WA 98195-5351.E-mail: parker@ocean.washington.edu

top ▲